PNAS RESEARCH ARTICLE | NEUROSCIENCE

Orange/far-red hybrid voltage indicators with reduced phototoxicity enable reliable long-term imaging in neurons and cardiomyocytes

Shuzhang Liu[a,b,1], Jing Ling[c,d,1], Peng Chen[e,f], Chang Cao[a], Luxin Peng[a], Yuan Zhang[d], Guangshen Ji[g], Yingna Guo[g], Peng R. Chen[a,c], Peng Zou[a,b,c,h,2], and Zhixing Chen[c,d,e,f,2]

Edited by Martin J. Schnermann, NIH, Frederick, MD; received April 28, 2023; accepted July 12, 2023 by Editorial Board Member Jeremy Nathans

Hybrid voltage indicators (HVIs) are chemogenetic sensors that combines the superior photophysical properties of organic dyes and the genetic targetability of protein sensors to report transient membrane voltage changes. They exhibit boosted sensitivity in excitable cells such as neurons and cardiomyocytes. However, the voltage signals recorded during long-term imaging are severely diminished or distorted due to phototoxicity and photobleaching issues. To capture stable electrophysiological activities over a long time, we employ cyanine dyes conjugated with a cyclooctatetraene (COT) molecule as the fluorescence reporter of HVI. The resulting orange-emitting HVI–COT–Cy3 enables high-fidelity voltage imaging for up to 30 min in cultured primary neurons with a sensitivity of ~ −30% $\Delta F/F_0$ per action potential (AP). It also maximally preserves the signal of individual APs in cardiomyocytes. The far-red-emitting HVI–COT–Cy5 allows two-color voltage/calcium imaging with GCaMP6s in neurons and cardiomyocytes for 15 min. We leverage the HVI–COT series with reduced phototoxicity and photobleaching to evaluate the impact of drug candidates on the electrophysiology of excitable cells.

chemo-genetic voltage indicators | phototoxicity | long-term imaging

In recent years, voltage imaging has emerged as a practical technique for detecting the spatial and temporal dynamics of electrical signals in neural circuits. Compared to traditional patch-clamp methods, voltage imaging has the combined advantages of noninvasive detection, high spatial resolution, simplicity of operation, and high throughput (1–4). An ideal voltage indicator should be bright, sensitive, and readily targetable to genetically specified cell subtypes. In recent imaging practice, high photostability and low phototoxicity are increasingly recognized as key parameters that are pivotal in high-fidelity long-term voltage imaging (5, 6).

Despite a proliferation of voltage indicators over the past decade, few can withstand long-term imaging for more than 30 min (4, 5, 7). Genetically encoded voltage indicators (GEVIs) are often hampered by their limited brightness and/or pronounced photobleaching (8). Organic dyes, such as cyanine dyes, are generally brighter and less prone to photobleaching than most of the fluorescent proteins with similar spectra. However, organic voltage-sensing dyes lack cell-type specificity (9). The hybrid voltage sensors, which harness organic dyes that are labeled to genetically encoded protein scaffolds, are regarded as an emerging technology combining the superior optical properties of organic dyes and the targetability of GEVIs (10). Among the emerging chemogenetic voltage sensors (11–15), Voltron (and its newer versions) is devised by fusing *Acetabularia acetabulum* rhodopsin II (Ace2) mutant to HaloTag where the Janelia Fluor (JF) dyes were introduced via haloalkane ligand as fluorescence donors. It has enabled voltage imaging in mouse, zebrafish, and *Drosophila* (11, 14). Hybrid voltage indicators (HVIs) developed in our lab exhibit excellent sensitivity, variable spectra, and cell-type targetable properties, though at present these tools do not work in vivo because the dye and enzyme components do not cross the blood–brain barrier (16). HVI conjugates fluorescent dye via "probe incorporation mediated by enzyme" (PRIME) labeling and "inverse-electron-demand Diels–Alder cycloaddition" (IEDDA) reaction (17). A LplA acceptor peptide (LAP) as the ligation site, is inserted into the first extracellular loop of Ace2 for enhancing the Förster resonance energy transfer (FRET) efficiency between fluorophore (donor) and rhodopsin (acceptor). HVI responds to the change of membrane potential in an electrochromic FRET mechanism (18), in which the fluorescence of HVI decreases when the cell depolarizes (Fig. 1*A*). However, in our previous work, phototoxicity was observed in HVIs labeled with cyanine dyes, which restricted their applications in voltage imaging for no longer than 10 min (16).

Significance

Voltage imaging is an emerging technology that captures electrical activities at single-cell resolution in a "noninvasive" manner. However, phototoxicity can hamper the long recording of vulnerable neurons. To extend the time window of optical recording, it is desirable to design a fluorescent voltage indicator with enhanced photostability and minimal phototoxicity. In this study, we upgrade a hybrid voltage indicator (HVI) by bioorthogonal labeling with cyanine dyes equipped with a triplet-state quencher, cyclooctatetraene (COT). The resulting indicators, HVI–COT–Cyanines, exhibit superior sensitivities and less phototoxicity than the current chemogenetic sensors. Our voltage indicators enable high-fidelity long-duration imaging in neurons and cardiomyocytes, representing capable tools for electrophysiological and pharmacological studies.

Author contributions: S.L., J.L., P.R.C., P.Z., and Z.C. designed research; S.L., J.L., P.C., and C.C. performed research; P.C., L.P., Y.Z., G.J., and Y.G. contributed new reagents/analytic tools; S.L., J.L., and L.P. analyzed data; and S.L., J.L., P.Z., and Z.C. wrote the paper.

The authors declare no competing interest.

This article is a PNAS Direct Submission. M.J.S. is a guest editor invited by the Editorial Board.

[1]S.L. and J.L. contributed equally to this work.

[2]To whom correspondence may be addressed. Email: zoupeng@pku.edu.cn or zhixingchen@pku.edu.cn.

This article contains supporting information online at https://www.pnas.org/lookup/suppl/doi:10.1073/pnas.2306950120/-/DCSupplemental.

Published August 17, 2023.

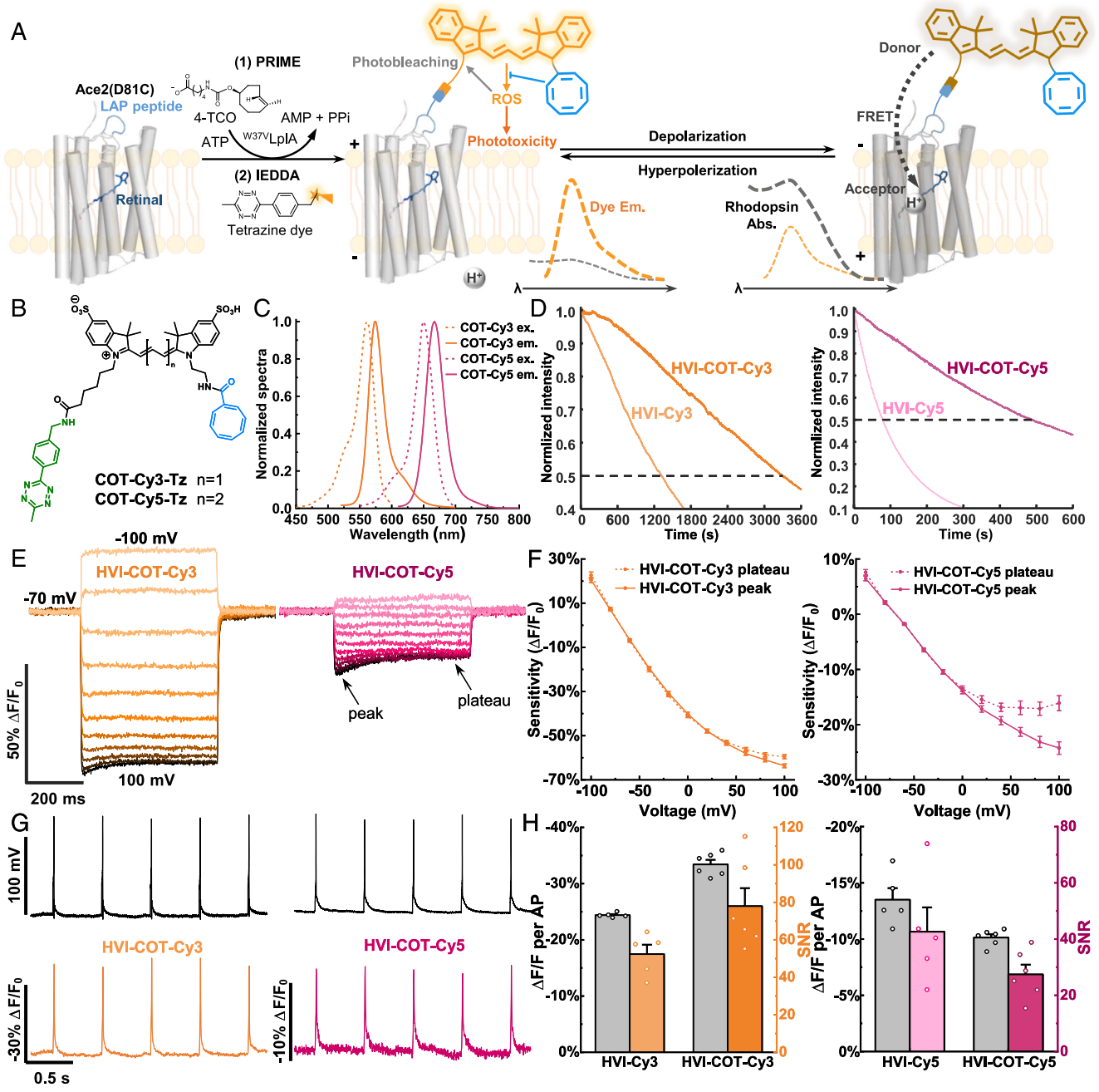

Fig. 1. Design and characterizations of HVI–COT–Cy3 and HVI–COT–Cy5. (*A*) Scheme for the mechanisms of fluorophore labeling, voltage sensing, photobleaching, and phototoxicity of HVI. HVI achieves fluorophore conjugation via two-step labeling methods. In the first step, an engineered lipoic acid ligase mutant (^{W37V}LplA) introduces *trans*-cyclooctene substrate (4-TCO) to LAP peptide. In the second step, tetrazine dye reacts with 4-TCO in a click manner. (*B*) Chemical structures of COT–Cy3–Tz and COT–Cy5–Tz. (*C*) Tetrazine dyes were reacted with equimolar 4-TCO and their excitation and emission spectra were measured in Tyrode's buffer. (*D*) Photostability comparison between HVI–COT–cyanine dyes and HVI–cyanine dyes labeled on fixed cells. Representative normalized photobleaching curves of HVI–COT–Cy3/HVI–Cy3 (*Left*), and HVI–COT–Cy5/HVI–Cy5 (*Right*) at 10 Hz. The illumination intensities of 532 nm and 637 nm lasers were 8 W•cm^{-2} and 2 W•cm^{-2}, respectively. (*E* and *F*) Voltage sensitivities characterization of HVI–COT–Cy3 and HVI–COT–Cy5 on HEK293T cells. (*E*) Representative fluorescence response of HVI–COT–Cy3 (*Left*) and HVI–COT–Cy5 (*Right*) to a series of step waveforms from −100 mV to 100 mV in increments of 20 mV applied by whole-cell patch clamp. (*F*) Voltage-fluorescence change plots. Responses were normalized to the fluorescence at −70 mV. Error bars represent SEM. (*G* and *H*) Sensitivities of HVI–COT–Cy3 and HVI–COT–Cy5 in neurons. (*G*) Representative single trial recordings of APs and fluorescence responses of HVI–COT–Cy3 (*Left*) and HVI–COT–Cy5 (*Right*) in neurons. Image sampling rates were 484 Hz. (*H*) AP sensitivities and SNR comparison of HVI–COT–Cy3/HVI–Cy3 (*Left*) and HVI–COT–Cy5/HVI–Cy5 (*Right*). The illumination intensities of 532 nm and 637 nm lasers were 5 W•cm^{-2} and 1.5 W•cm^{-2}, respectively. Error bars represent SEM.

Phototoxicity is a fundamental issue for fluorophores in optical imaging. It derives from the excited triplet state of fluorophores that generate reactive oxygen species (ROS) by interacting with oxygen from the environment. The phototoxicity produced from voltage imaging not only destroys the chromophore structure, leading to photobleaching, but also causes oxidative damage to biomolecules, such as membrane components, resulting in cell death (19–23). In the field of voltage imaging at a high frame rate (typically >500 Hz), the high excitation intensity required for achieving an adequate signal-to-noise ratio (SNR) would further aggravate ROS-induced photobleaching and phototoxicity. Moreover, the membranous structures are particularly prone to

ROS attack (6). Triplet state quenchers (TSQs), such as cyclooctatetraene (COT) or water-soluble vitamin E analogue (Trolox), can be added into the imaging buffer to reduce the phototoxicity from fluorophores by reducing ROS production rate (24, 25). Based on this photochemistry, it has been demonstrated that covalently conjugating TSQ to fluorophores, particularly cyanine dyes, can both improve photostability via intramolecular charge separation–independent triplet–triplet energy transfer (TET) (26–29) and alleviate the phototoxicity in live-cell imaging (30, 31). In addition, previous work (19, 32) demonstrated that COT-linked fluorophores tended to exhibit the broadest and most substantial improvement in photostability and phototoxicity. Recently, this strategy has been applied to reduce the phototoxicity of a green VoltageFluor (VF) dye, enabling 10-min imaging on cardiomyocytes (6). We reason that once engineered to a less phototoxic version, the state-of-the-art hybrid voltage sensor HVI would offer more appealing tools owing to their superior brightness and voltage sensitivity, cell specificity, and preferred spectra window in the far-red region for multiplexed imaging.

By upgrading the cyanine fluorophores to their COT conjugates, we present HVIs with markedly reduced phototoxicity and improved photostability (Fig. 1*A*). HVI–COT–Cy3 could record neuronal spike activities for 30 min with a sensitivity of approximately −30% $\Delta F/F_0$ per AP and could reflect the electrophysiological effects of drugs on neurons and cardiomyocytes. HVI–COT–Cy5 also achieved continuous imaging on neurons for 15 min with a sensitivity of around −6 to −10% $\Delta F/F_0$ per AP, while offering two-color calcium/voltage recording.

Result

Design and Characterization of HVI-COT-Dyes. We first synthesized conjugatable Cy3 and Cy5 with COT, the selected triplet-state quencher. Starting with water-soluble di-sulfo cyanine dyes, COT was introduced by amide coupling on one side (30), and the tetrazine (Tz) conjugation handle was introduced on the other alkyl chain of the cyanine dyes to give COT–Cy3–Tz and COT–Cy5–Tz (Fig. 1*B* and *SI Appendix*, *Methods*). The absorption and emission spectra of COT–Cy3–Tz and COT–Cy5–Tz were similar to the spectra of cyanine dyes without COT modification (Fig. 1*C* and *SI Appendix*, Table S1). ROS ($^1O_2$) generation measurement showed that COT-modified fluorophores had lower $^1O_2$ quantum yield than the corresponding cyanine dyes (*SI Appendix*, Fig. S1 and Table S1). There might be ROS other than $^1O_2$ that contributed to phototoxicity, which we have not been able to exhaustively measure due to the lack of convincing assays. Then, we moved to cellular labeling experiments to introduce COT-modified dyes to HEK293T cells transiently expressing HVI. We optimized dye concentration and labeling time to obtain an ideal brightness of the HVI sensor. Labeling with 1.5 μM COT–Cy3–Tz for 15 min was sufficient to saturate the labeling intensity (*SI Appendix*, Fig. S2).

We then characterized the photostability and phototoxicity of HVI–COT–Cy3 and HVI–COT–Cy5. Photobleaching curves were measured on formaldehyde-fixed HEK293T cells to prevent depolarization or deformation brought by phototoxicity. The bleaching half-life ($t_{1/2}$) of HVI–COT–Cy3 and HVI–COT–Cy5 were 2.4 and 5.6 times as much as HVI–Cy3 and HVI–Cy5 (Fig. 1*D* and *SI Appendix*, Table S2), respectively. Using whole-cell patch-clamp recording, we tested the membrane resistance, membrane capacitance, resting potential, amplitude of action potential (AP), rheobase, and AP full width of half maximum (FWHM) of the neurons expressing HVI–COT–Cy3 or HVI–COT–Cy5 with or without illumination. All of the electrophysiology properties had no significant difference between the groups in the presence and absence of illumination (*SI Appendix*, Fig. S3). The results suggest that HVI–COT–Cy3 (HVI–COT–Cy5) enables continuous imaging in neurons for 30 min (15 min) under the 1.5 W•cm^{-2} (0.8 W•cm^{-2}) excitation without compromising the measured cellular properties. In contrast, it was reported that the membrane resistance of neurons expressing HVI–Cy3 significantly decreased after 10 min excitation at 1 W•cm^{-2}. Notably, the illumination dose in previous work was only ~20% as much as this research (16). Altogether, we demonstrated that the COT conjugation significantly improved photostability and markedly alleviated the phototoxicity of HVI sensors.

Next, we measured the voltage sensitivities of HVI–COT–Cy3 and HVI–COT–Cy5 in HEK293T cells via a voltage clamp. HVI–COT–Cy3 had a huge sensitivity of −52.0 ± 1.1% $\Delta F/F_0$ per 100 mV (from −70 mV to 30 mV, *SI Appendix*, Table S3). The fluorescent responses to a series of step waveforms revealed that HVI–COT–Cy3 and HVI–COT–Cy5 were more sensitive to hyperpolarization (Fig. 1*E*). Besides, they had a visible hysteretic phenomenon when the membrane potential exceeded 40 mV, and the average of transient and steady-state responses of them was plotted separately (Fig. 1 *E* and *F*). Similar properties were observed in other rhodopsin-based voltage indicators (11, 33). AP sensitivities and the brightness of HVI–COT–Cy3 and HVI–COT–Cy5 in neurons were also measured. HVI–COT–Cy3 had an excellent sensitivity (−33.4 ± 0.8% $\Delta F/F_0$ per AP), representing the most sensitive orange-emitting voltage indicator to date. Such sensitivity well compensated its lower basal brightness (~70% of HVI–Cy3) and overall exhibited a remarkable signal-to-noise ratio (SNR = 78.0 ± 9.6), which were ~40% higher than HVI–Cy3 (Fig. 1*G* and *H* and *SI Appendix*, Fig. S4 and Table S3). The AP sensitivity (−10.1 ± 0.3% $\Delta F/F_0$ per AP), SNR (27.4 ± 3.5), and brightness of HVI–COT–Cy5 were lower than those of HVI–Cy5 (Fig. 1 *G* and *H* and *SI Appendix*, Fig. S4 and Table S3). Nevertheless, we slightly increased the illumination intensity to offset the decreased brightness of HVI–COT–Cy3, and HVI–COT–Cy5 has demonstrated superiority in subsequently continuous or discontinuous long-term functional imaging in neurons and cardiomyocytes thanks to its boosted photostability and gentle phototoxicity.

Long-Term Voltage Imaging in Neurons. By taking advantage of the low phototoxicity and good photostability of HVI–COT–Cy3, we aim to achieve voltage imaging for 30 min in neurons. After six rounds of 5-min imaging, the neurons expressing HVI–COT–Cy3 did not visibly alter morphology (Fig. 2*A*). Statistical analysis revealed no significant difference in spontaneous AP frequency among the six rounds of imaging, suggesting that HVI–COT–Cy3 did not change the excitability of neurons during 30 min imaging at 1.5 W•cm^{-2} 532 nm illumination (Fig. 2*B*). However, when the neuron expressing HVI–Cy3 was illuminated for more than 10 min, the spontaneous AP was significantly dropped and eventually stopped with the accumulation of phototoxicity (Fig. 2*C*).

Then, several drugs affecting neuronal excitability were treated before each round of recording. These drugs included gabazine, a competitive antagonist of $GABA_A$ receptors; cyclothiazide, a positive allosteric modulator of AMPA receptors that induces epileptiform burst (34); D-APV, an NMDA receptor antagonist; and NBQX, a competitive AMPA receptor antagonist. HVI–COT–Cy3 could report bursts of AP and subthreshold depolarization with excellent sensitivity and SNR throughout the imaging, which allows for the precise distinction of the effects on neuronal firing rate and interspike interval from drugs (Fig. 2*D* and *SI Appendix*, Fig. S5). For instance, gabazine or

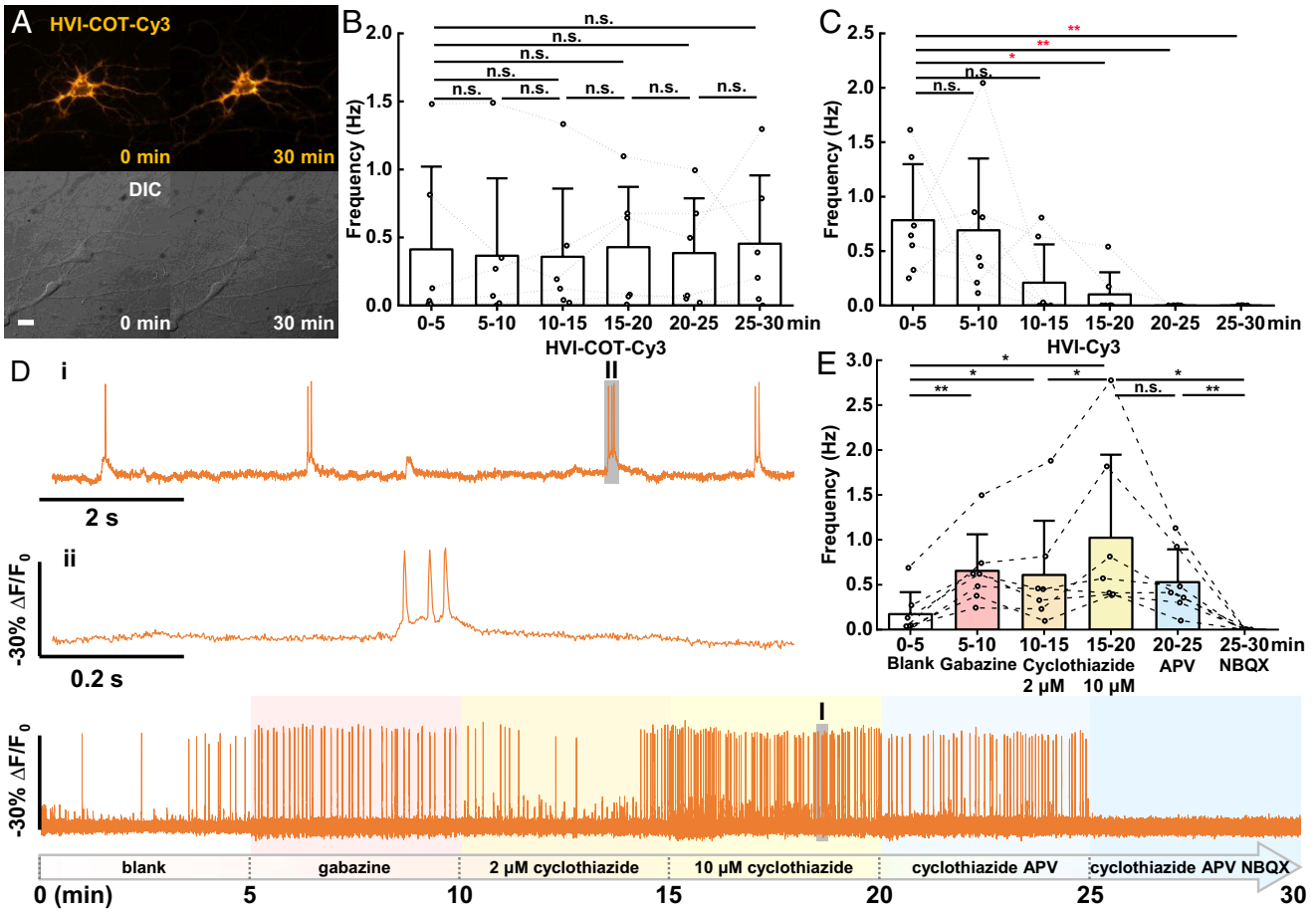

Fig. 2. HVI–COT–Cy3 enables 30-min long-term voltage imaging (720,000 frames) in neurons. (*A*) Wide-field imaging of neuron expressing HVI–COT–Cy3 before/after continuous illumination. (Scale bar, 20 μm.) (*B* and *C*) Statistics of AP burst frequency in cultured neurons during six rounds of 5-min voltage imaging. Imaging was performed for each neuron expressing HVI–COT–Cy3 (*B*, n = 6 cells) or HVI–Cy3 (*C*, n = 7 cells). Statistical significances are determined by one-way repeated measures ANOVA. (*D*) Drugs were treated before each round of recording: 20 μM gabazine was treated before the 2nd round and was replaced by 2 μM cyclothiazide before the 3rd round, cyclothiazide was additionally added to 10 μM before the 4th round, then 25 μM APV and 10 μM NBQX were added successively in the last two rounds. The signal of HVI–COT–Cy3 was photobleaching corrected. Two zoomed-in signals (i and ii) from two shaded regions (I and II) were presented on the top. The illumination intensity of the 532 nm laser was 1.5 W•cm^{-2}, and the camera frame rate was 400 Hz. (*E*) Statistics of AP frequency during each round of recording with drug treatment (n = 7 cells). Statistical significances are determined by a two-sided paired *t* test (*P < 0.05, **P < 0.01; n.s., not significant). Error bars represent SD.

cyclothiazide treatment increased neuronal firing rate; 2 μM or 10 μM cyclothiazide could enhance AP frequency to varying degrees; spontaneous AP of neurons was only partially inhibited after APV treatment, and the firing rate went down to zero after the addition of NBQX (Fig. 2*E*). Therefore, HVI–COT–Cy3 offered continuous monitoring of neurons responding to chemical stimuli over a long time.

HVI–Cy5 was introduced for crosstalk-free simultaneous imaging in neurons with GFP-based indicators such as calcium sensor, neurotransmitter sensor, and pH sensor due to the far-red spectra of Cy5. However, the poor photostability and underlying phototoxicity of Cy5 limit the imaging duration of HVI–Cy5 to less than 5 min (16). Neurons expressing HVI–Cy5 were imaged five times for 3 min each (a total of 15 min), and spontaneous AP frequency was significantly changed during the imaging process. After 9-min illumination, 75% of neurons no longer generated AP. On the contrary, HVI–COT–Cy5 is a superior substitution for HVI–Cy5 that did not show a significant difference in AP frequency among the five rounds of imaging (*SI Appendix*, Fig. S6 *A* and *B*). Hence, HVI–COT–Cy5 achieved dual-color imaging with GCaMP6s for 15 min at 0.8 W•cm^{-2} 637 nm illumination (Fig. 3 *A* and *B*).

During continuous imaging, we noted a gradual decay of sensitivity of HVI–COT–Cy5 (Fig. 3*B*). The averaged sensitivity in the 15th min was approximately 40% lower than that in the 1st min (Fig. 3*C*). Former electrophysiology experiments proved that 15-min illumination did not significantly alter the AP amplitude and FWHM in HVI–COT–Cy5 expressing neurons (*SI Appendix*, Fig. S3). Hence, we have ruled out phototoxicity as the cause of the reduction in AP sensitivity. The decayed sensitivity, combined with photobleaching, lead to the reduction of AP SNR (Fig. 3*C*). Nevertheless, HVI–COT–Cy5 was much less phototoxic than HVI–Cy5 and thus outperformed HVI–Cy5 in long-term dual-color imaging in neurons.

Optical Reporting of Electrical Activity in Cardiomyocytes. Next, we applied HVI–COT–Cy3 to record electrical signals in cardiomyocytes. HVI–COT–Cy3 expressing cardiomyocytes were barely bleached after performing imaging for a total of 30 min (Fig. 4 *A* and *B* and *SI Appendix*, Fig. S5). Notably, HVI was fast enough to report complete AP of ventricular myocytes from phase 0 (rapid depolarization) to phase IV (resting state, Fig. 4*C*). However,

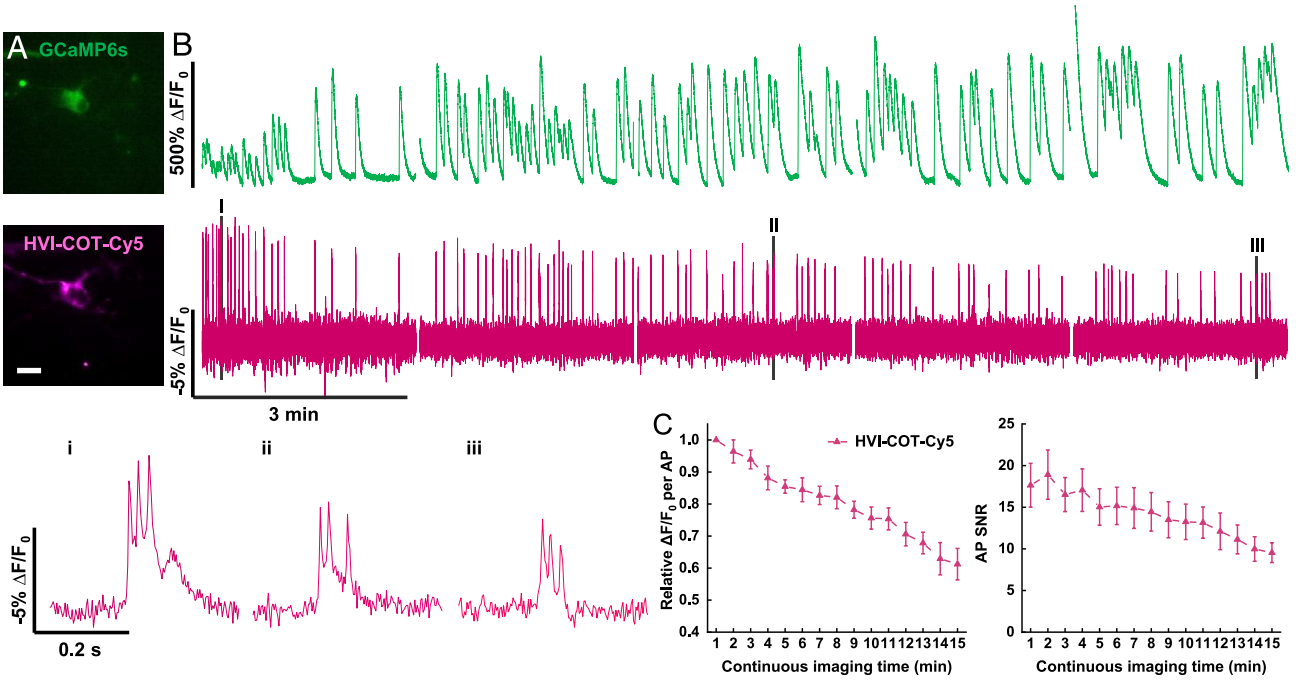

Fig. 3. HVI–COT–Cy5 enables 15-min simultaneous imaging with GCaMP6s in neurons. (*A*) Wide-field imaging of neuron coexpressing GCaMP6s–NES and HVI–COT–Cy5. (Scale bar, 20 μm.) (*B*) Dual-color imaging of calcium (green, 40 Hz) and voltage (magenta, 400 Hz) in neurons for 15 min in total. The signal of HVI–COT–Cy5 was photobleaching corrected. Zoomed-in signals (i–iii) of shaded regions (I–III) were plotted at the bottom. The illumination intensities of 488 nm and 637 nm lasers were 0.2 W•cm^{-2} and 0.8 W•cm^{-2} individually. (*C*) Relative sensitivity (*Left*) and SNR (*Right*) of HVI–COT–Cy5 (n = 6 cells) as a function of continuous imaging time. Error bars represent SEM.

voltage indicators with slow kinetics, such as ArcLight, only showed a transition between phase II (plateau) and phase IV (35).

Cardiomyocytes are particularly susceptible to phototoxicity and the accumulation of oxidative damage could significantly change their AP form, including AP amplitude and AP duration (APD) (6). Therefore, we carefully evaluated the impact of the phototoxicity of HVI on cardiomyocytes. Although cardiomyocytes expressing HVI–COT–Cy3 or HVI–Cy3 did not have an impact on the AP firing rate during the imaging process (*SI Appendix*, Fig. S6 *C* and *D*), the sensitivity, APD_{50}, and APD_{90} were significantly changed (Fig. 4 *C* and *D*). These phenomena implied that the form of AP in cardiomyocytes was cumulatively affected by phototoxicity. Furthermore, the AP sensitivity of HVI–Cy3 decayed much faster than HVI–COT–Cy3. After continuous imaging for 20 min, the sensitivity of HVI–Cy3 reduced by ~60% while that of HVI–COT–Cy3 decreased by ~28% (Fig. 4*D*). This result suggested that the decay of AP sensitivity was a result of both phototoxicity-induced reduction of AP amplitude in cardiomyocytes and the inherent decrease of HVI response (Fig. 3*C*). Even though HVI–COT–Cy3 had less phototoxicity than HVI–Cy3, it might not be suitable for reporting drug effects on AP form of cardiomyocytes in the format of continuous imaging. To avoid changing the AP duration of cardiomyocytes during imaging with HVI–COT–Cy3, and to investigate the influence of 30-min cell culture at room temperature on electrophysiology properties of cardiomyocytes at the same time, we designed an alternative imaging mode, consisting of two rounds of 3-min imaging with 30 min interval, shortening the total time of imaging to 6 min. In this "interval imaging" mode, the normalized ΔF of HVI–COT–Cy3 from two rounds of imaging were highly consistent (Fig. 4*E*). Except for a ~17% reduction in sensitivity after the whole part of imaging, average APD_{50} and APD_{90} were narrowed by no more than 6% and 4%, respectively (Fig. 4*F*). On the contrary, HVI–Cy3 had a ~32% decay in AP sensitivity, a ~32% decrease in APD_{50}, and an 18% increase in APD_{90}, differing greatly from those of continuous imaging for 6 min (Fig. 4 *D* and *F*). The results indicated that phototoxicity, rather than cell culture at room temperature, was the major factor for the changing of cellular electrophysiology parameters; the impact of accumulated phototoxicity on AP form became more apparent after a period of cell culture; and HVI–COT–Cy3 had little effects on AP duration and AP frequency of cardiomyocytes in interval imaging mode, surpassing HVI–Cy3.

The importance of interval imaging with HVI–COT–Cy3 is attributed to two aspects. On the one hand, it is capable of imaging cells before and after drug treatment from several regions of interest (ROI) successively in 30 min, increasing the throughput of a single pharmacological experiment by voltage imaging. On the other hand, it enables the assessment of drugs with relatively slow kinetics at dozens of minutes.

By introducing the interval imaging approach, we validated the impact of caffeine on the electrical activities of cardiomyocytes. As an adenosine A1 receptor antagonist and Ryanodine receptor (RyR) activator, Caffeine could regulate cardiomyocyte activity and even induce tachycardia by promoting calcium release from the sarcoplasmic reticulum (36). According to the results, 50 μM caffeine significantly increased AP frequency, dramatically narrowed APD_{50} by ~21%, and had no obvious effect on APD_{90} (Fig. 4 *G* and *H* and Movie S1), which is consistent with the previous reports (37, 38). Hence, by combining new imaging formats with intervals, HVI–COT–Cy3 could report the drug effects on AP frequency and duration of cardiomyocytes with high fidelity.

Finally, we performed spontaneous imaging of HVI–COT–Cy5 and GCaMP6s in cardiomyocytes for 15 min in total (Fig. 5 *A* and *B*). There were still no significant changes in spontaneous AP

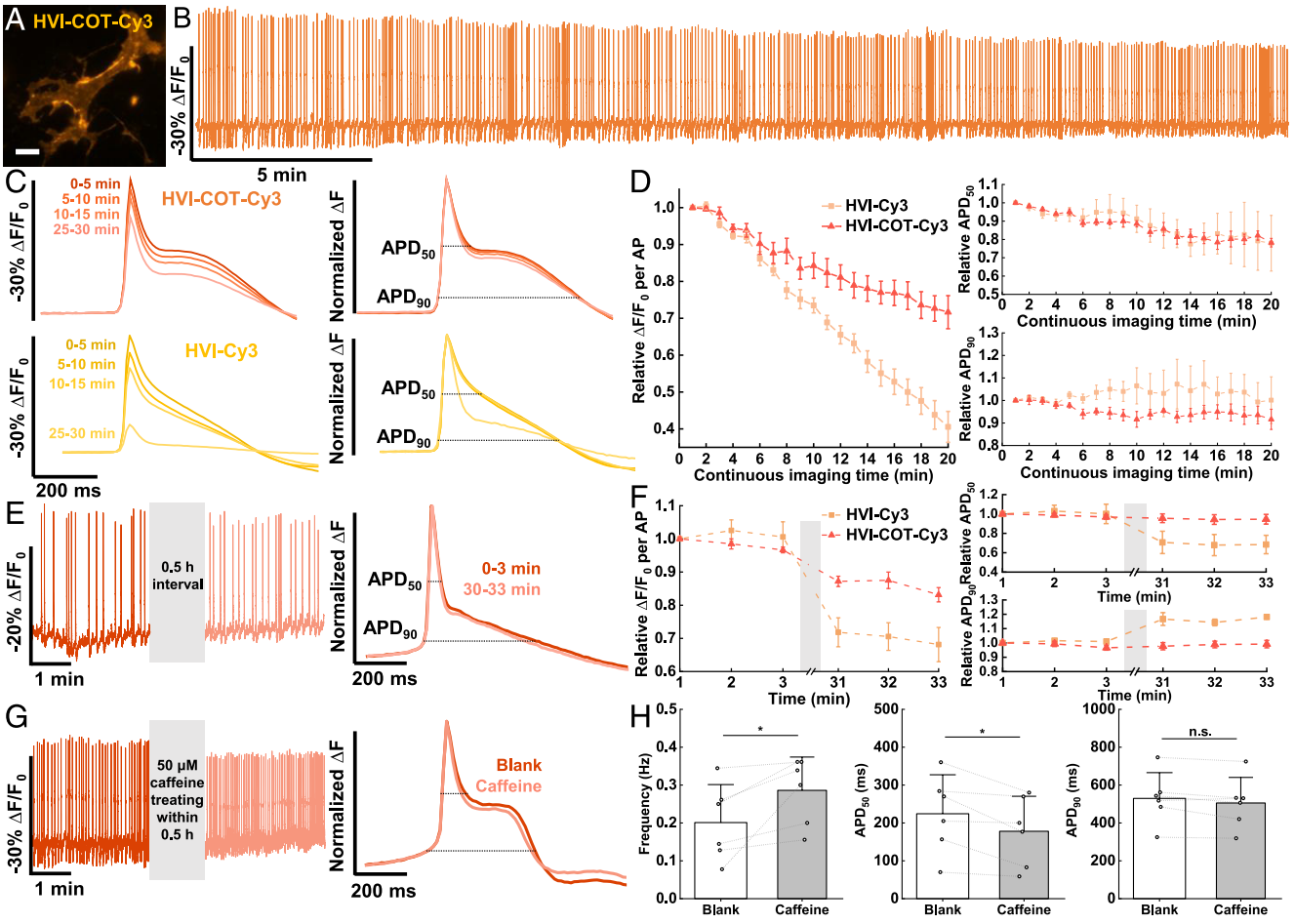

Fig. 4. HVI–COT–Cy3 responds to cardiac AP with high fidelity. (*A*) Wide-field imaging of cardiomyocyte expressing HVI–COT–Cy3. (Scale bar, 20 μm.) (*B*) Six rounds of 5-min voltage imaging were performed successively for each cardiomyocyte. The signal of HVI–COT–Cy3 was photobleaching corrected. The illumination intensity of the 532 nm laser was 1.5 W•cm^{-2}, and the camera frame rate was 100 Hz. (*C*) Overlays of the average AP signals (*Left*) and normalized average ΔF (*Right*) from four rounds of recording in *B*. (*D*) AP sensitivity, APD_{50}, and APD_{90} of HVI–COT–Cy3 (n = 7 cells) and HVI–Cy3 (n = 8 cells) as a function of continuous imaging time. (*E*) Two rounds of 3-min imaging were performed with a 30-min interval. (*F*) AP sensitivity, APD_{50}, and APD_{90} of HVI–COT–Cy3 (n = 9 cells) and HVI–Cy3 (n = 5 cells) as a function of time. Error bars represent SEM. (*G*) 50 μM caffeine was treated within 30-min interval. (*H*) Statistics of AP frequency, APD_{50}, and APD_{90} from the recording of blank and caffeine treatment (n = 6 cells). Error bars represent SD. Statistical significances are determined by a two-sided paired *t* test (*$P < 0.05$; n.s., not significant).

frequency during the imaging of the cardiomyocytes expressing HVI–COT–Cy5 or HVI–Cy5 (*SI Appendix*, Fig. S6 *E* and *F*), but the AP sensitivity, APD_{50}, and APD_{90} of HVI–COT–Cy5 and HVI–Cy5 varied a lot, similar to the performances of HVI–COT–Cy3 and HVI–Cy3 in cardiomyocytes (Fig. 5 *C* and *D*). In the HVI–COT–Cy5 group, during continuous imaging for 10 min, the average sensitivity decreased by ~12%, the absolute change of average APD_{50} was under 3%, and the APD_{90} widened less than 13%. In contrast, after 10-min imaging, the cardiomyocytes expressing HVI–Cy5 had a ~52% decay in sensitivity, a ~41% decrease in APD_{50}, and a ~45% drop in APD_{90} (Fig. 5*D*). Together, HVI–COT–Cy5 had much fewer side effects on cardiomyocyte electrophysiology properties than HVI–Cy5 and opened new possibilities in long-term dual-color imaging in cardiomyocytes without evident signal distortion.

Discussion

In summary, we report that COT-modified cyanine–tetrazine dyes, COT–Cy3–Tz and COT–Cy5–Tz, upgrade the photobiocompatibility and photostability of HVI. HVI–COT–Cy3 shows the highest sensitivity among orange voltage indicators, surpassing HVI–Cy3. Moreover, HVI–COT–Cy3 allows continuous voltage imaging for up to 30 min in neurons, as well as tracking drug effects on spike activities of neurons and cardiomyocytes. Meanwhile, HVI–COT–Cy5 also extends the voltage imaging window to 15 min in neurons, and it is orthogonal to green fluorescent indicators for the multiplexed evaluation of drug effects on neurons or cardiomyocytes.

We have also performed side-by-side comparisons between HVI–COT–Cyanine and Voltron2 series. HVI–COT–Cy3 and HVI–COT–Cy5 have higher sensitivities than the Voltron2 counterparts with similar spectra (i.e., $Voltron2_{525}$ and $Voltron2_{635}$). Besides, HVI–COT–Cy3 is over 40 times more photostable than $Voltron2_{525}$. $Voltron2_{525}$ is sufficiently bright to report neuronal AP with remarkable SNR in a short time (−11.8 ± 1.6% $\Delta F/F_0$ per AP, SNR = 41.2 ± 7.9, *SI Appendix*, Table S3). However, after 15 min, both photobleaching and underlying phototoxicity prevail (*SI Appendix*, Fig. S7 and Table S2).

From the phototoxicity perspective, this work adds to the few initiatives to alleviate photodamage using chemical approaches. Our understanding of photodamage is still preliminary. For instance, the voltage sensitivity of HVI in neurons and cardiomyocytes decreased during the continuous imaging process (Figs. 3 *B* and *C* and 4 *B*–*D*).

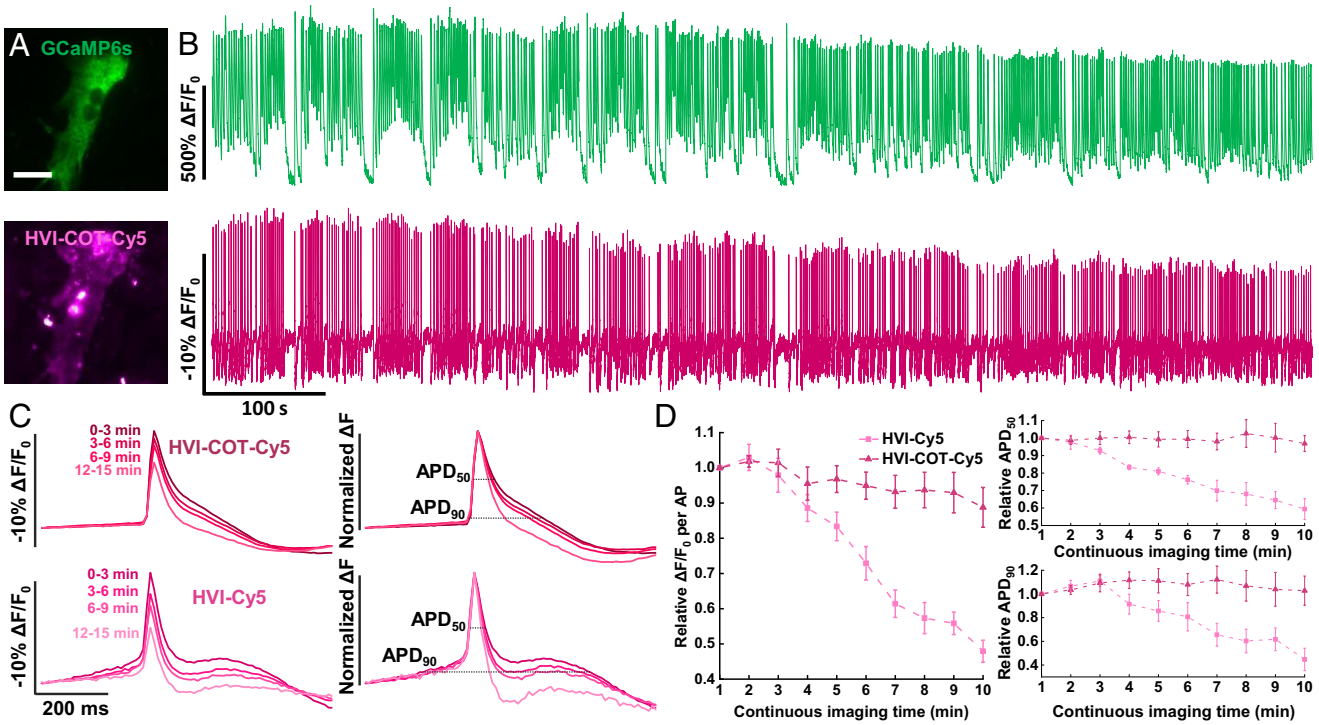

Fig. 5. HVI–COT–Cy5 is capable of long-term imaging with GCaMP6s in cardiomyocytes. (*A*) Wide-field imaging of cardiomyocyte coexpressing GCaMP6s–NES and HVI–COT–Cy5. (Scale bar, 20 μm.) (*B*) Dual-color imaging in cardiomyocytes for 15 min in total (488 nm channel: 0.1 W•cm^{-2}, 10 Hz; 637 nm channel: 0.8 W•cm^{-2}, 100 Hz). The signal of HVI–COT–Cy5 was photobleaching corrected. (*C*) Overlays of the average AP signals (*Left*) and normalized average ΔF (*Right*) from four rounds of 3-min recording in *B*. (*D*) AP sensitivity, APD_{50}, and APD_{90} of HVI–COT–Cy5 (n = 8 cells) and HVI–Cy5 (n = 7 cells) as a function of continuous imaging time. Error bars represent SEM.

These intriguing behaviors of voltage probes should prompt us to appreciate the chemistry of phototoxicity and inspire new approaches to eliminate such damages. From the perspective of eFRET sensors, HVI–COT–Cyanine had different sensitivities from HVI–Cyanine, even though the spectra of Cyanine and COT–Cyanine were almost identical (Fig. 1*C* and *SI Appendix*, Table S1). HVI–COT–Cyanine was slightly dimmer than HVI–Cyanine (*SI Appendix*, Fig. S4), hinting at additional photophysical processes in both singlet and triplet excited states. Given that the labeling method and the specific site of ligation remained the same, we hypothesized that the fluorophores exhibit different orientations, which affects FRET efficiency and voltage sensitivity. This phenomenon inspired us to open up a new direction for optimizing the hybrid voltage indicators.

While the current HVIs are not yet applicable to in vivo imaging due to the enzymatic labeling step, we foresee that HVI–COT–Cyanine palette will play an instrumental role in performing voltage imaging at longer time windows and at additional multiplexed channels. Restricted by photobleaching and phototoxicity, it was not practical for conventional voltage indicators, such as HVI–Cy3, to achieve imaging for more than 10 min with ideal SNR. By extending the imaging time window to 30 min, HVI–COT–Cy3 expands the variety of pharmacological experiments performed on the same cell samples. For example, add drugs to assess the effect on neuronal excitability and then withdraw them to observe the recovery; investigate the synergistic or antagonistic effect of multiple drugs on neural activity; investigate the drug onset concentration by setting up concentration gradient experiments; etc. Conducting such experiments on the same cell samples prevents variation from the heterogeneity of parallel groups of primary cells. For instance, AP forms from cultured cardiomyocytes have cell-to-cell variability (*SI Appendix*, Fig. S8). Moreover, membrane potential and calcium signal are two of the key indexes of cardiomyocyte functions. Recent research has focused on combining calcium imaging with patch-clamp techniques to identify the physiological activities of cardiomyocytes for drug screening or toxicity evaluation of novel medications (39, 40). In the future, HVI–COT–Cy5 offers a convenient and effective tool for assessing cardiac toxicity in drug screening platforms in vitro via duplex imaging with calcium indicators.

Materials and Methods

PRIME Labeling. For PRIME-IEDDA labeling (17), transfected cells were rinsed with Tyrode's Salts Solution (M&C Gene Technology) and then incubated with Tyrode's solution containing 5 μM ^{W37V}LplA [purified from bacterial culture as previously described (41)], 100 μM 4-TCO (16), 1 mM ATP, and 1 mM magnesium acetate at 37 °C for 30 min. Cells were gently rinsed with Tyrode's buffer three times, and subsequently labeled with 0.5 to 1.5 μM tetrazine dyes in Tyrode's buffer for 10 to 15 min (for instance, 1.5 μM 15 min for COT–Cyanine–Tz, whose tetrazine group was methyl substituent, or 0.5 μM 10 min for H substituent Cyanine–Tz. IEDDA labeling kinetics is attributed to tetrazine substituents, methyl group slows down the reaction kinetics) (42). Excess reagents were removed from each well and the cells were rinsed another three times before voltage imaging.

Imaging Apparatus and Wide-Field Microscopy. All fluorescence imaging experiments were performed with an inverted fluorescence microscope (Nikon-TiE) equipped with a 40× 1.3 NA oil immersion objective lens, three laser lines (Coherent OBIS 488 nm, 532 nm, and 637 nm), and two scientific CMOS cameras (Hamamatsu ORCA-Flash 4.0 v2). The microscope, lasers, and cameras were controlled by LabVIEW (National Instruments, 15.0 version) software.

A dual-view device (Photometrics DV2) was utilized to divide the emission into far-red and green fluorescence channels for two-color simultaneous imaging. *SI Appendix*, Table S3 provides a summary of the filters and dichroic mirrors

utilized for the fluorescence indicators in this work. Images were captured using a camera on 2 × 2 pixel binning and a 100-ms exposure duration. Images were analyzed using ImageJ/Fiji (version 1.52d).

Electrophysiology. For single-cell electrophysiological recording, cultured neurons were incubated in Tyrode's buffer containing 20 μM gabazine, 10 μM NBQX, and 25 μM APV (Tyrode's buffer containing 50 nM 2-APB for HEK293T cells). The electrophysiological experiments were conducted at room temperature. Borosilicate glass electrodes (Sutter) were pulled to a tip resistance of 2.5 to 5 MΩ. The internal solution containing 125 mM potassium gluconate, 8 mM NaCl, 0.6 mM $MgCl_2$, 0.1 mM $CaCl_2$, 1 mM EGTA, 10 mM HEPES, 4 mM Mg-ATP, and 0.4 mM GTP·Na_2 (pH 7.3) was adjusted to 295 mOsm/kg with 1 M sucrose and injected into the glass electrode. The glass electrode's position was adjusted by a Sutter MP285 micromanipulator. An Axopatch 200B (Axon Instruments) amplifier was utilized to clamp the cells. Membrane potential data recorded from the amplifier were filtered by an internal 5-kHz Bessel filter and digitalized at 9681.48 Hz with a National Instruments PCIe-6353 data acquisition (DAQ) board.

Simultaneous Patch-Clamp and Optical Recording in Cultured Cells. The membrane potential was controlled by a whole-cell patch clamp. To characterize the dynamic range of voltage indicators in HEK293T cells, the membrane potential was stepped from −100 mV to 100 mV in 20 mV increments, lasting 500 ms for each step. Meanwhile, the fluorescence images were recorded at 1,058 Hz.

Neuronal single action potentials (AP) were stimulated by injecting 100 to 400 pA current for 10 ms into the cultured neurons. Fluorescent signals were acquired at 484 Hz camera frame rate with 2-by-2 binning.

More detailed methods including chemical synthesis of COT–Cy3–Tz and COT–Cy5–Tz, ROS generation measurement, cell culture and transfection, data analysis, and code availability statement are described in *SI Appendix*.

Data, Materials, and Software Availability. MATLAB code data have been deposited in GitHub (https://github.com/PKUCHEMZouLab/HVI) (16). All study data are included in the article and/or supporting information.

ACKNOWLEDGMENTS. We acknowledge funding from the Ministry of Science and Technology (2022YFA1304700, 2018YFA0507600, and 2021YFF0502904), the Beijing Municipal Science & Technology Commission (Project: Z221100003422013), the National Natural Science Foundation of China (32088101). P.Z. is sponsored by Bayer Investigator Award. We thank Prof. Shiqiang Wang for the guidance on cardiomyocyte isolation, and the NMR facility of the National Center for Protein Sciences at Peking University for assistance with data acquisition.

Author affiliations: [a]College of Chemistry and Molecular Engineering, Synthetic and Functional Biomolecules Center, Beijing National Laboratory for Molecular Sciences, Key Laboratory of Bioorganic Chemistry and Molecular Engineering of the Ministry of Education, Peking University, Beijing 100871, China; [b]IDG/McGovern Institute for Brain Research at Peking University, Beijing 100871, China; [c]Peking-Tsinghua Center for Life Science, Academy for Advanced Interdisciplinary Studies, Peking University, Beijing 100871, China; [d]College of Future Technology, Institute of Molecular Medicine, National Biomedical Imaging Center, Beijing Key Laboratory of Cardiometabolic Molecular Medicine, Peking University, Beijing 100871, China; [e]Peking University-Nanjing Institute of Translational Medicine, Nanjing 211800, China; [f]Genvivo Biotech, Nanjing 211800, China; [g]State Key Laboratory of Membrane Biology, College of Life Sciences, Peking University, Beijing 100871, China; and [h]Chinese Institute for Brain Research, Beijing 102206, China

1. Y. Xu, P. Zou, A. E. Cohen, Voltage imaging with genetically encoded indicators. *Curr. Opin. Chem. Biol.* **39**, 1–10 (2017).
2. V. H. Cornejo, N. Ofer, R. Yuste, Voltage compartmentalization in dendritic spines in vivo. *Science* **375**, 82–86 (2022).
3. H. Tian *et al.*, Video-based pooled screening yields improved far-red genetically encoded voltage indicators. *Nat. Methods* **20**, 1082–1094 (2023).
4. M. Kannan *et al.*, Dual-polarity voltage imaging of the concurrent dynamics of multiple neuron types. *Science* **378**, 8797 (2022).
5. Z. Liu *et al.*, Sustained deep-tissue voltage recording using a fast indicator evolved for two-photon microscopy. *Cell* **185**, 3408–3425 (2022).
6. V. Grenier *et al.*, Molecular prosthetics for long-term functional imaging with fluorescent reporters. *ACS Cent. Sci.* **8**, 118–121 (2022).
7. J. Platisa *et al.*, High-speed low-light in vivo two-photon voltage imaging of large neuronal populations. *Nat. Methods* **20**, 1095–1103 (2023).
8. Y. Bando, C. Grimm, V. H. Cornejo, R. Yuste, Genetic voltage indicators. *BMC Biol.* **17**, 71 (2019).
9. E. W. Miller, Small molecule fluorescent voltage indicators for studying membrane potential. *Curr. Opin. Chem. Biol.* **33**, 74–80 (2016).
10. S. Liu, J. Yang, P. Zou, Bringing together the best of chemistry and biology: Hybrid indicators for imaging neuronal membrane potential. *J. Neurosci. Methods* **363**, 109348 (2021).
11. A. S. Abdelfattah *et al.*, Bright and photostable chemigenetic indicators for extended in vivo voltage imaging. *Science* **365**, 699–704 (2019).
12. C. Deo *et al.*, The HaloTag as a general scaffold for far-red tunable chemigenetic indicators. *Nat. Chem. Biol.* **17**, 718–723 (2021).
13. P. E. Deal *et al.*, Covalently tethered rhodamine voltage reporters for high speed functional imaging in brain tissue. *J. Am. Chem. Soc.* **142**, 614–622 (2020).
14. A. S. Abdelfattah *et al.*, Sensitivity optimization of a rhodopsin-based fluorescent voltage indicator. *Neuron* **111**, 1547–1563.e9 (2023).
15. T. C. Alich *et al.*, A dark quencher genetically encodable voltage indicator (dqGEVI) exhibits high fidelity and speed. *Proc. Natl. Acad. Sci. U.S.A.* **118**, e2020235118 (2021).
16. S. Liu *et al.*, A far-red hybrid voltage indicator enabled by bioorthogonal engineering of rhodopsin on live neurons. *Nat. Chem.* **13**, 472–479 (2021).
17. D. S. Liu *et al.*, Diels-Alder cycloaddition for fluorophore targeting to specific proteins inside living cells. *J. Am. Chem. Soc.* **134**, 792–795 (2012).
18. P. Zou *et al.*, Bright and fast multicoloured voltage reporters via electrochromic FRET. *Nat. Commun.* **5**, 4625 (2014).
19. Z. Yang *et al.*, Cyclooctatetraene-conjugated cyanine mitochondrial probes minimize phototoxicity in fluorescence and nanoscopic imaging. *Chem. Sci.* **11**, 8506–8516 (2020).
20. D. E. Dolmans, D. Fukumura, R. K. Jain, Photodynamic therapy for cancer. *Nat. Rev. Cancer* **3**, 380–387 (2003).
21. K. Kassab, Photophysical and photosensitizing properties of selected cyanines. *J. Photochem. Photobiol. B Biol.* **68**, 15–22 (2002).
22. H. Sies, C. F. Menck, Singlet oxygen induced DNA damage. *Mutat. Res.* **275**, 367–375 (1992).
23. M. J. Davies, R. J. Truscott, Photo-oxidation of proteins and its role in cataractogenesis. *J. Photochem. Photobiol. B Biol.* **63**, 114–125 (2001).
24. R. Dave, D. S. Terry, J. B. Munro, S. C. Blanchard, Mitigating unwanted photophysical processes for improved single-molecule fluorescence imaging. *Biophys. J.* **96**, 2371–2381 (2009).
25. P. Palozza, N. I. Krinsky, Astaxanthin and canthaxanthin are potent antioxidants in a membrane model. *Arch Biochem. Biophys.* **297**, 291–295 (1992).
26. Q. Zheng *et al.*, On the mechanisms of cyanine fluorophore photostabilization. *J. Phys. Chem. Lett.* **3**, 2200–2203 (2012).
27. P. Tinnefeld, T. Cordes, "Self-healing" dyes: Intramolecular stabilization of organic fluorophores. *Nat. Methods* **9**, 426–427 (2012).
28. R. B. Altman *et al.*, Enhanced photostability of cyanine fluorophores across the visible spectrum. *Nat. Methods* **9**, 428–429 (2012).
29. R. B. Altman *et al.*, Cyanine fluorophore derivatives with enhanced photostability. *Nat. Methods* **9**, 68–71 (2011).
30. Q. Zheng *et al.*, Electronic tuning of self-healing fluorophores for live-cell and single-molecule imaging. *Chem. Sci.* **8**, 755–762 (2017).
31. T. Liu *et al.*, Multi-color live-cell STED nanoscopy of mitochondria with a gentle inner membrane stain. *Proc. Natl. Acad. Sci. U.S.A.* **119**, e2215799119 (2022).
32. Q. Zheng *et al.*, Ultra-stable organic fluorophores for single-molecule research. *Chem. Soc. Rev.* **43**, 1044–1056 (2014).
33. Y. Han *et al.*, Bright and sensitive red voltage indicators for imaging action potentials in brain slices and pancreatic islets. BioRxiv [Preprint] (2022). https://doi.org/10.1101/2022.12.01.518652 (Accessed 1 December 2022).
34. G. Woodruff *et al.*, Screening for modulators of neural network activity in 3D human iPSC-derived cortical spheroids. *PLoS One* **15**, e0240991 (2020).
35. J. S. Leyton-Mange *et al.*, Rapid cellular phenotyping of human pluripotent stem cell-derived cardiomyocytes using a genetically encoded fluorescent voltage sensor. *Stem. Cell Rep.* **2**, 163–170 (2014).
36. A. Zulli *et al.*, Caffeine and cardiovascular diseases: Critical review of current research. *Eur. J. Nutr.* **55**, 1331–1343 (2016).
37. Z. Qi *et al.*, Extracellular and intracellular angiotensin II regulate the automaticity of developing cardiomyocytes via different signaling pathways. *Front Mol. Biosci.* **8**, 699827 (2021).
38. R. Balasubramaniam, S. Chawla, A. A. Grace, C. L. Huang, Caffeine-induced arrhythmias in murine hearts parallel changes in cellular Ca^{2+} homeostasis. *Am. J. Physiol. Heart Circ. Physiol.* **289**, H1584–H1593 (2005).
39. S. Bedut, R. Kettenhofen, J. M. D'Angelo, Voltage-sensing optical recording: A method of choice for high-throughput assessment of cardiotropic effects. *J. Pharmacol. Toxicol. Methods* **105**, 106888 (2020).
40. G. T. Dempsey *et al.*, Cardiotoxicity screening with simultaneous optogenetic pacing, voltage imaging and calcium imaging. *J. Pharmacol. Toxicol. Methods* **81**, 240–250 (2016).
41. C. Uttamapinant, M. I. Sanchez, D. S. Liu, J. Z. Yao, A. Y. Ting, Site-specific protein labeling using PRIME and chelation-assisted click chemistry. *Nat. Protoc.* **8**, 1620–1634 (2013).
42. G. Beliu *et al.*, Bioorthogonal labeling with tetrazine-dyes for super-resolution microscopy. *Commun. Biol.* **2**, 261 (2019).